PHYSICAL REVIEW D **83,** 094013 (2011)

Off-shell effects for t-channel and s-channel single-top production at next-to-leading order in QCD

P. Falgari,[1] F. Giannuzzi,[2] P. Mellor,[3] and A. Signer[3]

[1]*Institute for Theoretical Physics and Spinoza Institute, Utrecht University, 3508 TD Utrecht, The Netherlands*
[2]*Dipartimento di Fisica, Università degli Studi di Bari, I-70126 Bari, Italy and I.N.F.N., Sezione di Bari, I-70126 Bari, Italy*
[3]*IPPP, Department of Physics, University of Durham, Durham DH1 3LE, England*

(Received 28 February 2011; published 10 May 2011)

In this work we present a calculation of both t-channel and s-channel single-top production at next-to-leading order in QCD for the Tevatron and for the LHC at a center-of-mass energy of 7 TeV. All the cross sections and kinematical distributions presented include leading nonfactorizable corrections arising from interferences of the production and decay subprocesses, extending previous results beyond the narrow-width approximation. The new off shell effects are found to be generally small, but can be sizeable close to kinematical endpoints and for specific distributions.

DOI: 10.1103/PhysRevD.83.094013 PACS numbers: 14.65.Ha

I. INTRODUCTION

The production of a single-top quark in hadronic collisions was observed, for the first time, two years ago by both the D0 and CDF collaborations at the Fermilab Tevatron [1,2]. Contrary to the top-pair production mechanism, which proceeds via strong interactions in the standard model (SM), single-top production is mediated by electroweak couplings, and thus represents an important window into the charged-current interactions of the top quark. Though experimentally challenging, due to the presence of large backgrounds from Wj and $t\bar{t}$ production, this process will play an important role in the physics program of the LHC, where top quarks will be produced at much higher rates than at the Tevatron. Measurements of the cross section allow for a direct determination of the CKM matrix element, V_{tb}, whose precise value provides a test of the unitarity of the weak-flavor mixing matrix [3]. Moreover, the angular correlations of the products of the top quark decay encode information on the spin structure of the Wtb vertex and on the production dynamics of the top quark [4,5], and can thus be used to set limits on the strength of possible anomalous couplings and new-physics effects [6,7]. Being sensitive to the bottom quark content of the proton, the single-top production cross section also encodes information on the bottom quark parton density, which so far has been theoretically computed from the gluon PDF, rather than extracted from experimental data. Finally, beside being an important signal in itself, single-top production also represents a background to a number of new-physics production channels, including some relevant for Higgs-boson searches [8]. For these reasons, an accurate theoretical understanding of single-top production is clearly desirable.

In the SM, a single-top quark can be produced via exchange of a virtual, t-channel W boson ($qb \to q't$ or $\bar{q}b \to \bar{q}'t$), a virtual, s-channel W boson ($q\bar{q}' \to t\bar{b}$) or in association with a real W ($bg \to W^- t$). At the Tevatron, the largest contribution to the cross section comes from the t-channel process, followed by s-channel production, whereas associated Wt production is negligible. At the LHC, the t-channel production process still dominates the cross section, but the associated production mechanism gives the second largest contribution, while the s-channel cross section is very small (see, e.g., Ref. [9]). Note that the distinction of t-channel and s-channel production is somewhat artificial since, starting at next-to-leading-order (NLO) in QCD, both processes can give rise to the same physical final state. While, from a theoretical point of view, the two channels can always be disentangled on a diagram-by-diagram basis, depending on the sign of the invariant mass of the intermediate W boson, experimentally they are defined by two distinct sets of selection criteria and kinematical cuts, chosen in such a way to suppress one of the two processes in favor of the other. However, as it will be shown in more detail in Sec. III, for some observables the contribution of the "wrong" channel can still be sizeable, even after cuts. For this reason, a detailed phenomenological analysis generally requires the inclusion of both t-channel and s-channel production. The associated production of a top quark with a W boson produces very different final-state topologies and, experimentally, its signal can be much more easily disentangled from the other two channels. Hence, in the following we will ignore this production mechanism and focus our attention on t-channel and s-channel single-top production only.

Both t-channel and s-channel single-top production have been studied extensively in the literature. The NLO corrections to both channels, as well as Wt associated production, have been known for a while [10–14], and a fully differential calculation was presented in Refs. [15,16]. Electroweak corrections, both in the SM and in the MSSM, have also been computed and appeared in more recent works [17,18], while resummation of soft-gluon corrections was studied in, among others, Refs. [19,20] using the Mellin-space formalism, and Refs. [21,22] using

 © 2011 American Physical Society

renormalization-group techniques in the context of soft-collinear effective theory. All these works considered the case of a stable top quark, ignoring the subsequent decay of the top to lighter, longer-lived particles.

The decay of the top quark can be included in the, so-called, narrow-width approximation (NWA), where the top is produced on shell and then allowed to decay. This approach allows for the inclusion of realistic cuts on the decay products of the top quark and preserves spin correlations between initial and final states. Also, the complexity of the calculation is only sightly increased compared to the stable-quark approximation. In the NWA framework, NLO corrections correspond to the, so-called, *factorizable* corrections, i.e. (on shell) corrections to either the production or decay subprocess. NLO QCD analyses in this framework for the semileptonic top decay were published in Refs. [23–26] and, more recently, with an extended and detailed phenomenological analysis in Refs. [27,28].

None of the works mentioned so far have included *nonfactorizable* corrections, i.e. contributions from virtual and real gluons connecting production and decay subprocesses. Such off shell effects were studied recently in Ref. [29], for t-channel single-top production, where the fully differential cross section was computed for a *resonant* ($p_t^2 - m_t^2 \sim m_t\Gamma_t$), rather than on shell ($p_t^2 - m_t^2 = 0$), top quark. A similar calculation for s-channel production was presented in Ref. [30] and nonfactorizable corrections to other processes have been considered as well [31,32]. We should mention that apart from nonfactorizable corrections one has to consider also so-called background diagrams, i.e. diagrams with the same final state but with no intermediate top quark. This has been done for t-channel single-top production in Ref. [29] and for $t\bar{t}$ production at hadron colliders in Ref. [33].

The effective-theory approach adopted in Ref. [29] will be reviewed briefly in Sec. II. Here it is sufficient to say that the effect of nonfactorizable corrections was found to be generally small for inclusive-enough observables, consistent with previous calculations [34,35], though they can be locally sizeable near kinematic thresholds and for specific distributions.

Here we extend the results of Ref. [29] to the s-channel production mechanism, getting an overall view of the process, and present a more detailed analysis of the size of these off shell effects. We also discuss how the t-channel and s-channel mechanisms can be experimentally identified. All the results presented in Sec. III include nonfactorizable corrections and, in most cases, the corresponding prediction in the narrow-width approximation is given for comparison. In our calculation we adopt the 5-flavor scheme, setting the bottom quark mass to zero. The relation between the 5-flavor and 4-flavor scheme has been extensively studied in Refs. [36,37]. Furthermore, we generally take the CKM matrix to be the unit matrix. However, in Sec. III C we will briefly discuss how CKM-suppressed initial-state configurations can significantly modify the shape of the top-rapidity distribution, as first observed by the authors of Ref. [38] for the tree-level processes. Finally, in the present calculation we do not include the matching of the NLO result and parton shower Monte Carlo. This was implemented in the programs MC@NLO [39,40] and POWHEG [41,42].

The paper is organized as follows: In Sec. II we will review the effective-theory formalism, introduced in Ref. [29], for the calculation of the nonfactorizable corrections to t-channel single-top production, and illustrate the (trivial) extensions necessary to include the s-channel process. In Sec. III we will first give the precise selection rules and kinematical cuts we used to define t-channel-like and s-channel-like signatures, and then present cross sections and relevant kinematical distributions for the Tevatron (in Sec. III A) and for the 7 TeV LHC (in Sec. III B). This section also contains a discussion of the scale dependence of the NLO results and, as previously mentioned, a brief discussion of the importance of CKM off diagonal partonic channels. Finally, in Sec. IV we draw our conclusions.

II. CALCULATION

In Ref. [29] a formalism was presented that allows for the systematic inclusion of nonfactorizable and background contributions to the production of a massive, unstable particle. The method discussed there is based on a previously developed framework [43] in which the heavy-resonance production is described in an effective-theory (ET) language. Here we limit ourselves to a brief review of this method and refer the reader to Refs. [29,43] for more detail.

A. The ET approach to unstable-particle production

The key point of the approach adopted here is the relaxation of the assumption made in the narrow-width approximation of an exactly on shell massive-particle, $p_X^2 = m_X^2$, where m_X denotes the mass of the particle, for the moment generically referred to as X. Instead we consider a *resonant*, unstable particle with a nonvanishing virtuality, $p_X^2 - m_X^2 \neq 0$, which is assumed to be much smaller than the unstable-particle mass, $p_X^2 - m_X^2 \ll m_X^2$. The hierarchy between the virtuality and the mass of the unstable particle provides a small parameter, $D_X/m_X^2 \equiv (p_X^2 - m_X^2)/m_X^2$, from which a systematic expansion of the full matrix element is performed. In this respect, the effective-theory approach to unstable-particle production can be seen as a systematization and extension of the pole approximation [44,45]. To make this hierarchy explicit, we introduce a generic small parameter, $\delta \ll 1$, and count $D_X/m_X^2 \sim \delta$.

In the effective theory, only low-virtuality modes with $q^2 \lesssim m_X^2\delta^2$ are still dynamical, and are described by a set of effective fields. These include, in particular, a *resonant* field, Φ_X, to describe the heavy, unstable particle; *collinear*

fields, ψ_c, describing massless, energetic particles; and *soft* fields, A_s, corresponding to low-scale gluonic fluctuations. The effects related to the nonvanishing width of particle X are resummed into the leading, massive-particle kinetic term of the effective Lagrangian:

$$2\hat{M}_X \phi_X^\dagger \left(i v \cdot \partial - \frac{\Omega_X}{2} \right) \phi_X, \tag{2.1}$$

where the coefficient, Ω_X, can be related to $\bar{s} = m_X^2 - i m_X \Gamma_X$, the gauge invariant complex pole of the full heavy-particle propagator [43].[1] *Hard* modes with virtuality of order m_X^2 are not part of the effective Lagrangian. Their effect is instead included in the effective-theory calculation through hard matching coefficients, i.e. effective couplings extracted from fixed-order, on shell matrix elements of the full theory. Note that in this context, "on shell" refers to the complex pole of the heavy-particle propagator, i.e. $p_X^2 = \bar{s} \equiv m_X^2 - i m_X \Gamma_X$, meaning that the couplings of the effective Lagrangian are generally complex. This is a feature shared with the Complex Mass Scheme, in which the gauge invariant resummation of finite-width effects is obtained through a complex renormalization of masses and couplings of the SM Lagrangian [46].

From a practical point of view, the hard matching coefficients and the effective-theory matrix elements required can be easily computed using the method of regions (see Refs. [47,48]) to expand, in powers of δ, the loop integrals of the full theory. In the *hard region*, the integrand is expanded under the assumption that the loop momentum, q, scales as $q \sim m_X$. Hard corrections coincide with what, in the language of the double-pole approximation, are usually defined as factorizable corrections, i.e. corrections that can unambiguously be assigned to the production or decay of the unstable particle. On the other hand, the loop corrections in the effective theory encode nonfactorizable effects, and can be obtained from the *soft part* of full loop integrals, computed by expanding the integrand according to the assumption that the loop momentum scales as $q \sim m_X \delta$. The correspondence between a strict effective-theory calculation and the expansion by regions is schematically given in Fig. 1. Note that the separation of hard and soft corrections is gauge invariant and can, in principle, be pursued to an arbitrarily-high number of loops [49].

For the total cross section, real radiative corrections can be treated as virtual ones, using the optical theorem to relate phase space integrals to loop integrals and expanding with the method of regions. In this context, the effective-theory formalism has been previously applied to linear-collider phenomenology [50,51]. For an arbitrary observable, the inclusion of real corrections in the effective-theory formalism poses some problems. First of all, the method of regions relies on dimensional regularization to take care of possible extra singularities introduced by the expansion in δ, whereas real corrections in high-energy physics calculations are typically computed numerically in $D = 4$ dimensions. Furthermore, in the presence of an extra gluon with momentum q in the final state, it is, *a priori*, not clear what the correct expansion parameter is, given that both p_X^2 and $(p_X - q)^2$ can become resonant. Finally, an arbitrary observable introduces, in general, new scales that can hamper the effective-theory expansion in δ.

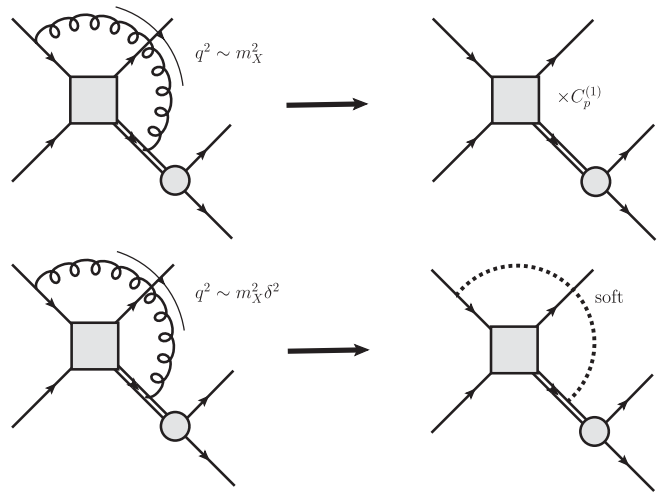

FIG. 1. Correspondence between the expansion by regions and the effective-theory calculation: hard loops (top left) coincide with corrections to the matching coefficient of the production vertex (top right), whereas soft loops (bottom left) reproduce the effect of loop diagrams in the effective theory (bottom right).

For the aforementioned reasons, in Ref. [29] we deviated from a strict ET calculation and used the full matrix element to compute real corrections. This can, in principle, pose a problem since the different treatment of virtual and real corrections could lead to uncanceled infrared singularities in the cross section. The cancellation of infrared singularities is usually made manifest by adding and subtracting from the NLO cross section a suitably chosen term that correctly reproduces the soft and collinear singularities of the real matrix element:

$$\begin{aligned} d\sigma^{\rm NLO} &= d\sigma_V + \int d\Phi d\sigma_R \\ &= \left(d\sigma_V + \int d\Phi d\sigma_{\rm subt} \right) + \int d\Phi (d\sigma_R - d\sigma_{\rm subt}), \end{aligned} \tag{2.2}$$

where $d\sigma_V$ and $d\sigma_R$ denote virtual and real corrections, respectively, and $d\Phi$ represents the integration over the phase space of the additional final-state particle. The first term in the second line of Eq. (2.2) is integrated analytically in $D = 4 - 2\epsilon$ dimensions, ideally leading to an explicit cancellation of the poles in ϵ, whereas the second term, which is free of singularities by construction, can be

[1] In the pole scheme that we are using in this paper, one has the simple relation $\Omega_X = -i\Gamma_X$.

computed numerically in $D = 4$ dimensions. In our case, the virtual-correction term, $d\sigma^V$, is expanded in δ, neglecting terms that are suppressed by $\mathcal{O}(\alpha_s\delta)$ with respect to the leading-order term, resulting in $d\sigma_V^{\rm exp}$. This also modifies the infrared poles of the virtual corrections and the singularities of the subtraction term in Eq. (2.2) do not cancel with the infrared singularities of $d\sigma_V^{\rm exp}$. An exact cancellation of the singularities requires that $d\sigma_{\rm subt}$ in the first term of Eq. (2.2) is also expanded consistently, i.e.

$$d\sigma^{\rm NLO} \sim \left(d\sigma_V^{\rm exp} + \int d\Phi d\sigma_{\rm subt}^{\rm exp}\right) + \int d\Phi(d\sigma_R - d\sigma_{\rm subt}). \tag{2.3}$$

Given that the kinematical configurations described by $d\sigma_{\rm subt}$ correspond to a gluon being soft or two partons being collinear, in this case the expansion parameter can always be clearly identified. Note that Eq. (2.3) is formally gauge invariant as long as $d\sigma_R$ contains the full set of relevant Feynman diagrams. Furthermore, the neglected terms are suppressed by $\alpha_s\delta$ with respect to the leading-order term.

B. *t*-channel and *s*-channel single-top production

In Ref. [29] the effective-theory formalism just described was applied to t-channel single-top production. In this work we extend that calculation to include the s-channel production mechanism. At the Born level we are thus interested in the three processes:

$$\begin{aligned} &t\text{-channel} \qquad q(p_1)b(p_2) \to q'(p_3)b(p_4)W^+(p_W),\\ &\bar{q}'(p_1)b(p_2) \to \bar{q}(p_3)b(p_4)W^+(p_W),\\ &s\text{-channel} \qquad q(p_1)\bar{q}'(p_2) \to \bar{b}(p_3)b(p_4)W^+(p_W), \end{aligned} \tag{2.4}$$

where $(q, q') \in \{(u, d), (c, s)\}$. The leptonic decay, $W^+(p_W) \to e^+(p_5)\nu_e(p_6)$, is included in the narrow-width approximation and, in the following, will be understood. In this article we will not give explicit results for the production of an antitop, $\bar{t}$, but our results could, of course, be trivially extended to this case. Along the same lines as the calculation presented in Ref. [29], we systematically expand the amplitudes for these processes in the small parameters α_s, α_{ew} and $\Delta_t \equiv (p_W + p_b)^2 - m_t^2 + im_t\Gamma_t$. Throughout the paper we will denote these parameters collectively as δ and assume the relative scaling

$$\delta \sim \alpha_s^2 \sim \alpha_{ew} \sim \frac{\Delta_t}{m_t^2}. \tag{2.5}$$

At tree-level, the amplitudes for the three processes (2.4) contain contributions from *resonant diagrams*, containing an intermediate top quark propagator, and nonresonant ones. The latter are further grouped into *electroweak nonresonant diagrams* and *QCD background diagrams*, in which two electroweak vertices are replaced by strong couplings. Accordingly, the amplitude for $qb \to q'bW^+$ can be parameterized as [29]

$$\mathcal{A}^{\rm tree} = \delta_{31}\delta_{42}(g_{ew}^3 A_{(-1)}^{(3,0)} + g_{ew}^3 A_{(0)}^{(3,0)} + \ldots) + T_{31}^a T_{42}^a g_{ew} g_s^2 A^{(1,2)}, \tag{2.6}$$

where the powers of the strong and electroweak couplings associated with the amplitude have been made explicit and appear as upper indices, whereas a lower index denotes a power of the resonant propagator Δ_t, i.e. $A_{(k)}^{(i,j)} \sim (\Delta_t)^k$ and has a prefactor $g_{ew}^i g_s^j$. A similar representation holds for the processes $\bar{q}'b \to \bar{q}bW^+$ and $q\bar{q}' \to \bar{b}bW^+$, whose amplitudes can be obtained from the first t-channel process by crossing $p_1 \to -p_3$ and $p_2 \to -p_3$, respectively. The term $g_{ew}^3 A_{(-1)}^{(3,0)}$, which scales as $g_{ew}^3(\Delta_t)^{-1} \sim \delta^{1/2}$, arises from the leading contribution of the resonant diagram, whereas $g_{ew}^3 A_{(0)}^{(3,0)} \sim \delta^{3/2}$ accounts for subleading contributions from the same diagram, where the resonant propagator is cancelled by higher-order terms in δ, or from the electroweak background diagrams. The leading-order term of the matrix element squared thus scales as δ. The contribution of the QCD background diagrams is given by $g_{ew}g_s^2 A^{(1,2)} \sim \delta$, i.e. they are, in principle, suppressed by only $\delta^{1/2} \sim \alpha_s \sim 10\%$ compared to the leading resonant contribution. However, the interference between these diagrams and the resonant diagram does not contribute to the squared matrix element due to the different color structure of the QCD and purely EW contributions. Thus, at Born level, the first corrections to the matrix element squared are suppressed by a factor δ and not $\delta^{1/2}$.

While terms of $\mathcal{O}(\delta^{3/2})$ in the cross section vanish at the Born level, terms with this parametric scaling arise from a subset of one-loop QCD corrections and real-gluon corrections. These contributions are what, in the following, we define as our NLO approximation. The one-loop diagrams are given by virtual corrections to the resonant tree-level diagram. Note that only upon expansion in δ is this subset of corrections gauge invariant. The leading term in the expansion in Δ_t/m_t^2, given by the sum of leading soft and hard contributions, was computed in Ref. [29] for the t-channel production processes. Again, the analogous result for the s-channel process can be obtained via the replacement $p_2 \leftrightarrow -p_3$.

While Eq. (2.3) requires the use of the full, unexpanded matrix element for the process $qb \to q'bW^+g$ for the computation of real corrections, here we include only a subset of diagrams corresponding to gluonic corrections to the resonant electroweak diagram. This allows us to avoid the calculation of real corrections to background diagrams, but in general violates gauge invariance. However, the omitted diagrams, missing a resonant top propagator, are numerically suppressed by an extra power of δ. This is also the case for the gauge-violating effects, as long as the condition $\Delta_t^2/m_t^2 \ll 1$ is satisfied. We would like to stress

that the approximation made here is not a limitation of the method, but a choice made out of convenience, which could be easily relaxed. In practise, we use the real-correction amplitudes given in Ref. [29], where in the numerator of the amplitudes m_t^2 was replaced by $\bar{s}$. This actually restores gauge invariance but, from a numerical point of view, does not significantly improve the approximation.

Alongside the aforementioned real diagrams, corrections from gluon-initiated partonic processes also contribute to the NLO cross section. More precisely, one has to include the processes

$$gb \to q\bar{q}'bW^+, \qquad qg \to q'\bar{b}bW^+, \qquad \bar{q}'g \to \bar{q}\,\bar{b}\,bW^+.$$

The required matrix elements can be obtained by suitably crossing the results for the process $qb \to q'bW^+g$, given in Ref. [29]. While the first process can be unambiguously assigned to t-channel top production, the processes with a bottom and antibottom in the final state can arise from diagrams with a W boson exchanged in either the t or s channel. More precisely, the amplitude for the process $qg \to q'\bar{b}bW^+$ can be written as

$$\mathcal{A}_{qg}^{\text{tree}} = g_s g_{ew}^3 (T_{47}^{a_2}\delta_{31}A_{qg}^{47} + T_{31}^{a_2}\delta_{47}A_{qg}^{31}), \tag{2.7}$$

where the term proportional to A_{qg}^{47} is usually assigned to t-channel single-top production, and the term proportional to A_{qg}^{31} to s-channel production. As anticipated in the introduction, while this separation of the two channels on a diagram-by-diagram basis is possible from a theoretical point of view, in general both of them will contribute to an experimentally defined observable. This is discussed in detail and quantified in the next section.

III. RESULTS

As mentioned earlier, all necessary tree-level, virtual and real amplitudes for the t-channel processes were computed in Ref. [29]. The necessary amplitudes for s-channel single-top production can thus be obtained from there by crossing. These results were implemented in two independent Monte Carlo codes, one adopting the Catani-Seymour dipole subtraction scheme [52], and the other the FKS subtraction method [53].

In this section we will present results for the two hadronic processes:

$$N_1N_2 \to J_bJ_le^+E_T + X, \tag{3.1}$$

$$N_1N_2 \to J_bJ_{\bar{b}}e^+E_T + X, \tag{3.2}$$

where $N_1N_2 = p\bar{p}$ for Tevatron and $N_1N_2 = pp$ for LHC. J_b ($J_{\bar{b}}$) represents a jet generated from a bottom quark (antiquark), J_l is a jet generated from a light parton and E_T denotes missing transverse energy. Clearly, from an experimental point of view, jets generated from a bottom quark or antiquark are not distinguishable. This assumption can easily be relaxed, however, this is unessential to the discussion of nonfactorizable corrections, which is the main point of this work. In Eqs. (3.1) and (3.2), X represents an arbitrary number of additional jets which are not generated from b or $\bar{b}$ quarks.

Process (3.1) clearly represents a t-channel-like signature, while (3.2) represents an s-channel-like signal. In fact, at LO in QCD, only t-channel diagrams contribute to the cross section for (3.1) and (3.2) is determined by s-channel diagrams only. However, as mentioned at the end of Sec. II B, at NLO in QCD both production channels can contribute to both experimental signatures due to the mixing arising from the qg processes in Eq. (2.7). While the contribution of s-channel configurations to the first process is negligible, the t-channel contribution to $N_1N_2 \to J_bJ_{\bar{b}}e^+E_T + X$ can be numerically important, even after applying suitable cuts to suppress it. This is discussed more quantitatively in Sec. III A and III B.

The input parameters for our numerical analysis are given in Table I. The NLO top-decay width is used for both Born and next-to-leading-order cross sections. Within a strict effective-theory approach, in the leading part of the bilinear operator, Eq. (2.1), Ω_X corresponds to the leading-order width within the pole mass scheme. NLO corrections to the width (i.e. the matching coefficient Ω_X) would be taken into account perturbatively. However, we decided to resum NLO corrections to Ω_X as well. The difference between these two approaches is beyond $\mathcal{O}(\delta^{3/2})$ and our approach avoids large differences due to using different input parameters, which could obscure the effect of genuine NLO corrections. For the same reason, we use the MSTW2008 NLO PDF set [54] and the corresponding value of strong coupling, α_s, everywhere. Jets are constructed using a standard $k_\perp$ cluster algorithm with a resolution parameter $D_{\text{res}} = 0.7$, but any other jet definition could equally well be used. Unless otherwise specified, the renormalization and factorization scales are, by default, set to $\mu_R = \mu_F = m_t/2$.

A. Single-top production at the Tevatron

We start by presenting results for single-top production for proton-antiproton collisions at a center-of-mass energy of 1.96 TeV. The kinematical cuts and vetoes applied to the two processes, (3.1) and (3.2), are presented in Table II. In both cases we apply a (loose) constraint on the invariant mass of the $J_be^+\nu_e$ system, defined by

$$m_{\text{inv}}(t) = \sqrt{(p(J_b) + p(e) + p(\nu))^2}, \tag{3.3}$$

TABLE I. Input parameters used for calculating the cross sections and distributions shown in Sec. III A, III B, and III D.

$m_t = 172$ GeV	$\alpha_{ew} = 0.03394$
$M_W = 80.4$ GeV	$\Gamma_W = 2.14$ GeV
$M_Z = 91.2$ GeV	$\Gamma_t^{\text{NLO}} = 1.32813$ GeV

TABLE II. Kinematical cuts and vetoes used for Tevatron results.

$p\bar{p} \to J_b J_l e^+ \not{E}_T + X$	$p\bar{p} \to J_b J_{\bar{b}} e^+ \not{E}_T + X$
$p_T(J_b) > 20$ GeV	$p_T(J_b) > 20$ GeV
$p_T(\text{hardest } J_l) > 20$ GeV	$p_T(J_{\bar{b}}) > 20$ GeV
$p_T(\text{extra } J_{\bar{b}}) < 20$ GeV	$p_T(\text{extra } J_l) < 15$ GeV
$\not{E}_T + p_T(e) > 30$ GeV	$\not{E}_T + p_T(e) > 30$ GeV
$120 < m_{\text{inv}} < 200$ GeV	$120 < m_{\text{inv}} < 200$ GeV

where the three-momentum of the invisible neutrino can be exactly reconstructed by imposing an on shell condition for the $e^+\nu_e$ system, i.e. $(p(e) + p(\nu))^2 = M_W^2$. The cut on m_{inv} ensures that $\delta < 1$ and, thus, that the effective-theory counting is satisfied. Further standard cuts are applied on the transverse momenta of the b-tagged jet and the charged lepton, on the momentum of the hardest light jet in process (3.1) or the $\bar{b}$-tagged jet in process (3.2), and on the transverse missing energy, $\not{E}_T$. Finally, for the process $p\bar{p} \to J_b J_l e^+ \not{E}_T + X$ we impose a veto on extra b-tagged jets. This suppresses the contributions from the s-channel production diagrams, except for the kinematic configurations in which the $\bar{b}$ jet is very forward, and thus undetected. A similar veto is imposed on extra light jets in the process $p\bar{p} \to J_b J_{\bar{b}} e^+ \not{E}_T + X$ to suppress contributions from the t-channel diagrams. We would like to point out that our calculation is fully differential, and the cuts can, therefore, be easily varied at will. The cuts used here represent a minimal, but still realistic, setup that allows the discussion of nonfactorizable corrections.

Results for the total cross sections, for both the effective-theory calculation (ET) and the spin-correlated narrow-width approximation (NWA), are presented in Table III. As previously mentioned, the NLO top quark width and PDFs are used for both the LO and NLO cross sections. The total NLO corrections are large, and amount to $\sim -38\%$ and $\sim -21\%$ for $p\bar{p} \to J_b J_l e^+ \not{E}_T$ and $p\bar{p} \to J_b J_{\bar{b}} e^+ \not{E}_T$, respectively. As expected for the total cross section, both at LO and NLO the difference between the ET calculation, which includes nonfactorizable corrections, and the NWA result is small, amounting to $\sim$1.5%, which is compatible with the naïve expectation of the accuracy of the NWA, i.e. $\Gamma_t/m_t \sim 1\%$. For the process $p\bar{p} \to J_b J_l e^+ \not{E}_T + X$ about 96% of the NLO cross section is given by t-channel diagrams, whereas the s-channel contribution amounts to 4%. For $p\bar{p} \to J_b J_{\bar{b}} e^+ \not{E}_T + X$ the s-channel diagrams contribute about 87% of the NLO cross section. In this case the contamination from t-channel configurations is sizeable, even after applying cuts specifically designed to suppress it.

TABLE III. LO and NLO cross sections for the processes (3.1) and (3.2), computed using the parameters given in Table I and imposing the kinematical cuts and vetoes given in Table II. The errors come from scale uncertainty only. All numbers are in femtobarns.

$p\bar{p} \to J_b J_l e^+ \not{E}_T + X$		ET	NWA
	LO [fb]	$86.89(1)^{+0.45}_{-4.01}$	88.11(1)
	NLO [fb]	$53.62(5)^{+7.76}_{-15.24}$	54.43(1)
$p\bar{p} \to J_b J_{\bar{b}} e^+ \not{E}_T + X$		ET	NWA
	LO [fb]	$34.68(1)^{+3.53}_{-2.97}$	35.16(1)
	NLO [fb]	$27.42(2)^{+1.95}_{-1.00}$	27.79(1)

The errors on the values presented in Table III are obtained from scale variation only (the errors in parenthesis are statistical Monte Carlo errors), i.e. no PDF uncertainty is considered. Both renormalization and factorization scale are varied in the interval $m_t/4 \leq \mu_R = \mu_F \leq m_t$. The scale dependence from LO to NLO results is only moderately reduced for the $p\bar{p} \to J_b J_{\bar{b}} e^+ \not{E}_T$ process, whereas it is increased for $p\bar{p} \to J_b J_l e^+ \not{E}_T$. This is partly due to the renormalization-scale dependence of the NLO result, which is absent at LO since the resonant Born cross section does not depend on the strong coupling constant, α_s. This is better seen in Fig. 2, where several cross sections are shown as a function of the scale μ. The dashed red curve, obtained by varying the factorization scale in the NLO result while keeping the renormalization-scale fixed, is clearly flatter than the solid red curve, where the two scales were varied simultaneously. The plot also shows that the unusually small scale dependence of the LO results does not stem from using the NLO PDFs, since this affects the normalization of the result but not the shape. Furthermore, the scale uncertainty of the results depends quite strongly on the choice of the central value for μ, and our default choice lies close to the region where the scale dependence of the NLO result is stronger.

We would like to point out that, in a strict effective-theory approach, soft and hard contributions are typically renormalized at different scales, $\mu_s \ll \mu_h$, and then evolved to a common factorization/renormalization-scale, μ, using suitable renormalization-group equations. This evolution effectively resums large logarithms of the ratio $\ln\mu_s/\mu_h \sim \ln\Gamma_t/m_t \sim \ln\delta$, generally improving the scale dependence of the cross sections. In the approach used in this work, where real corrections are computed in the full theory, the application of the aforementioned procedure is problematic since the separation of real hard and soft contributions is not transparent. For this reason, in the present work we evaluate hard and soft contributions at the same scale $\mu = \mu_h$. Given that $\alpha_s(\mu_s)$ is substantially larger than $\alpha_s(\mu_h)$, this might lead to an underestimation of the importance of nonfactorizable corrections and it may, therefore, be worthwhile studying the effects of large-logarithm resummation for generic observables.

Next we consider the top invariant mass (defined in Eq. (3.3)) distributions which are plotted in Fig. 3. The two plots show results for the LO and NLO effective-theory predictions (blue and red bands, respectively) and

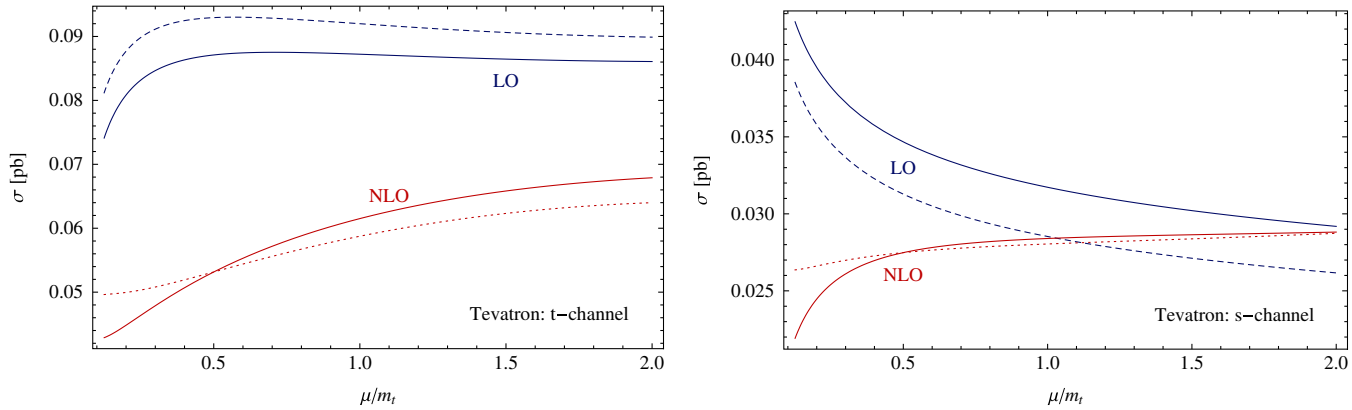

FIG. 2 (color online). Scale dependence of the total cross section for $p\bar{p} \to J_b J_l e^+ \not{E}_T$ (left) and $p\bar{p} \to J_b J_{\bar{b}} e^+ \not{E}_T$ (right) at the Tevatron. The plot shows the LO cross section with LO (dashed blue) and NLO (solid blue) PDFs, and the NLO cross section with simultaneous variation of factorization and renormalization scale (solid red) and for fixed factorization scale (dashed red).

for the NLO NWA result (green curve). The LO prediction in the NWA is a delta function centered at the top mass, and in the plot would show as a spike at $m_{\rm inv} = m_t$. The blue and red bands are obtained by varying the scales in the usual interval, $m_t/4 \leq \mu_R = \mu_F \leq m_t$, in the LO and NLO EFT results. The total NLO corrections are very large and negative in the peak region, $m_{\rm inv} \sim m_t$, whereas they are still large, but positive, in the tail region where the cross section is numerically very small due to the rapid Breit-Wigner falloff. The difference between the red and green curves, which gives the nonfactorizable and off shell effects, is relatively small far below and above the peak of the distribution. However, nonfactorizable corrections are large and negative at the peak (especially for the s-channel-like process), and large and positive immediately above it. The change in sign of nonfactorizable contributions around $m_{\rm inv}$ explains the small difference between the off shell and on shell predictions found in observables which are inclusive with respect to the top quark invariant mass, for example, the total cross section, discussed above. As was the case for the total cross section, close to the interesting region of the peak the scale dependence of the NLO ET result is only mildly reduced compared to the LO result for the process $p\bar{p} \to J_b J_{\bar{b}} e^+ \not{E}_T$ (the seemingly larger band shown in the central bin of the plot is an effect of the logarithmic scale), and is actually increased for the t-channel-like signal.

In Figs. 4 and 5 we present a selection of relevant kinematical distributions. For the process $p\bar{p} \to J_b J_l e^+ \not{E}_T + X$ (Fig. 4) we plot the following observables:

$$M_T(t) \equiv \sqrt{|\vec{p}_\perp(J_b)|^2 + |\vec{p}_\perp(e)|^2 + \not{E}_T^2 - (\vec{p}_\perp(J_b) + \vec{p}_\perp(e) + \vec{p}_\perp(\nu))^2}, \qquad H_T(J_b, J_h) \equiv |\vec{p}_\perp(J_b)| + |\vec{p}_\perp(J_h)|,$$
$$p_T(t) \equiv |\vec{p}_\perp(e) + \vec{p}_\perp(\nu) + \vec{p}_\perp(J_b)|, \qquad \eta(t) \equiv \frac{1}{2}\ln\left(\frac{|\vec{p}(t)| + |\vec{p}_\parallel(t)|}{|\vec{p}(t)| - |\vec{p}_\parallel(t)|}\right), \qquad M_{\rm inv}(e, \nu, J_h) \equiv \sqrt{(p(e) + p(\nu) + p(J_h))^2},$$
$$\cos\theta_S \equiv \frac{\vec{p}(e)\cdot\vec{p}(J_h)}{|\vec{p}(e)||\vec{p}(J_h)|}\bigg|_{\rm top\ r.f.}, \tag{3.4}$$

where $\vec{p}(t) = \vec{p}(J_b) + \vec{p}(e) + \vec{p}(\nu)$, the lower indices $\perp$ and $\parallel$ denote the momentum components perpendicular and parallel to the beam axis, $\vec{p}(\nu)$ and $\vec{p}_\perp(\nu)$ represent the missing total and missing transverse momenta, respectively, and J_h is the hardest, non-b-tagged jet. $M_T(t)$ represents the top quark transverse mass, $H_T(J_b, J_h)$ the hadronic transverse energy, $p_T(t)$ the transverse momentum of the reconstructed top quark, $\eta(t)$ the pseudorapidity of the top quark, $M_{\rm inv}(e, \nu, J_h)$ the invariant mass of the $e^+\nu_e J_h$ system, and $\cos\theta_S$ the angle between the charged lepton and the hardest light jet in the rest frame of the top quark. In all histograms the dark blue solid line represents the LO ET result for the central value of the scales, whereas the NLO result is given by the red solid line. The light blue and red bands are obtained by varying the factorization and renormalization scales in the interval $m_t/4 \leq \mu_R = \mu_F \leq m_t$, while the orange band comes from varying the factorization scale only in the NLO results, keeping the renormalization-scale fixed. The dashed magenta curve is the (unphysical) NLO result obtained by omitting the processes with a quark and gluon in the partonic initial state and both a b and $\bar{b}$ quark in the final state. This artificially removes any processes which could lead to a $\bar{b}$ jet in the final state, even if that jet would not be resolved, and acts as a perfect $\bar{b}$-jet veto. The black dot-dashed curve represents the (tree-level) QCD background.

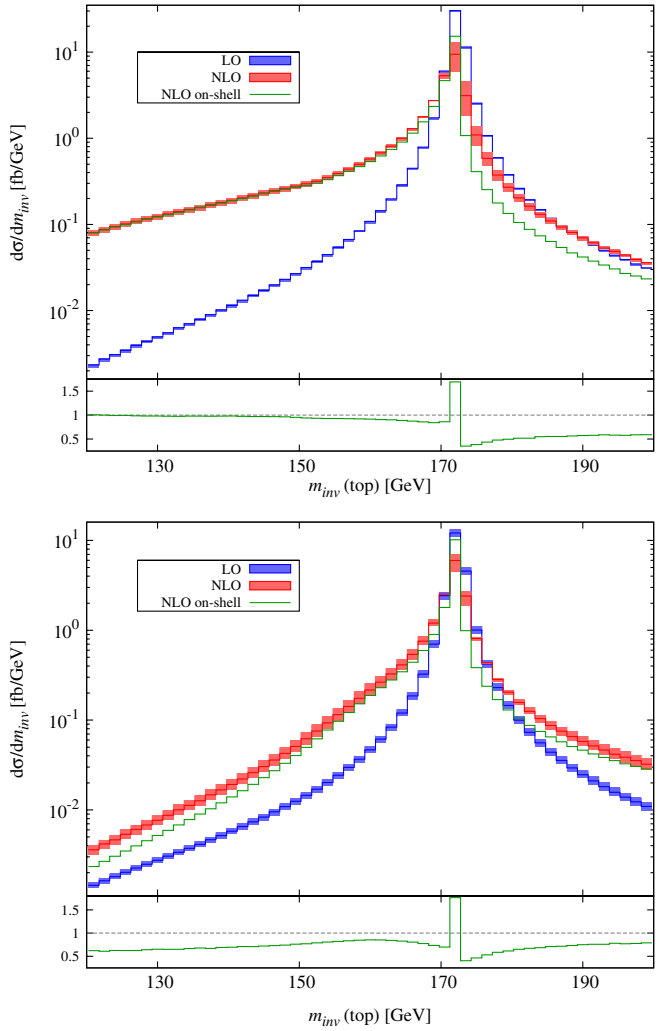

FIG. 3 (color online). Top invariant mass distributions for the process $p\bar{p} \to J_b J_l e^+ E_T + X$ (upper plot) and $p\bar{p} \to J_b J_{\bar{b}} e^+ E_T + X$ (lower plot) at the Tevatron. The blue band represents the LO ET result, the red band the NLO ET result, and the green curve the NLO spin-correlated NWA prediction. For the ET results the band width is obtained by varying the factorization and renormalization scales in the interval $m_t/4 \leq \mu_R = \mu_F \leq m_t$. The lower panels show the NWA result divided by the NLO ET result to illustrate the off shell effects.

The total NLO corrections are generally large and negative for the cuts used here, reaching up to 50% of the LO result depending on the distribution and on the bin chosen, though the shape of the distributions is usually only mildly modified. The bulk of the correction arises from the gluon-initiated partonic channels, as follows from comparing the solid red and dashed magenta lines. Nonfactorizable corrections are typically small. This is shown, in detail, in the bottom plots in Fig. 4. Here the ratio of the NWA result and the resonant result is given for two different implementations of the narrow-width approximation, one with exact spin correlations (solid green curve, right scale) and one without (dashed green curve, left scale). Off shell effects amount to about 2–3%, except close to the edges of particular distributions where they can be much larger (see, e.g., the plot for $M_T(t)$). It is interesting to note that spin-correlation effects can be much more important than nonfactorizable corrections. This is the case for the $p_T(t)$ distribution and for $\cos\theta_S$, whereas for other observables the difference between the two implementations of the NWA is small. To further illustrate the size of the spin-correlation effects in the $\cos\theta_S$ distribution, the NLO narrow-width-approximation result without spin-correlation is shown in Fig. 4 (dashed green curve, bottom right plot). Comparing this curve to the ET NLO curve (red) shows a dramatic change in the shape of the distribution.

Nonfactorizable effects are much smaller than one would naively expect from the result found for the invariant mass distribution, where off shell corrections at the peak are sizeable. This is partly due to an averaging effect which stems from the fact that, for a fixed value of a given observable, O, the top invariant mass, $m_{\rm inv}$, can, in general, vary over a large range of values. Consider, as an example, the top transverse mass distribution, $M_T(t)$. For a fixed value of $M_T(t)$, the top quark invariant mass varies in the interval $M_T(t) < m_{\rm inv} < 200$ GeV, where the upper cutoff follows from the cuts we imposed. Because of the change in sign of the off shell effects around the peak at $m_{\rm inv} = m_t$, for $M_T(t)$ smaller than the top mass, large cancellations between positive and negative corrections take place, leading to small nonfactorizable corrections for $M_T(t) \lesssim 160$ GeV. On the other hand, if $M_T(t) \gtrsim m_t$ the cancellations are less effective, explaining the relatively large off shell effects close to the distribution edge. A similar reasoning can also be applied to other observables.

In the plots in Fig. 4 we also show the contribution of QCD background diagrams, represented by the black dot-dashed curve. In the effective-theory counting these terms are of $\mathcal{O}(\delta^2)$, i.e. subleading compared to the $\mathcal{O}(\delta^{3/2})$ nonfactorizable corrections, and are thus expected to be numerically negligible. While this is true for some observables, like, for example, M_T and H_T, where the shape of the distribution for signal and background are qualitatively very different and peak in different kinematical ranges, for other, like $p_T(t)$ and $\eta(t)$, the shape of the QCD background is similar to the signal, and its size comparable to the contribution of NLO corrections. For $\cos\theta_S$ the QCD background contributes a constant shift of the distribution. The apparent breakdown in the effective-theory counting could possibly be explained by the fact that the relation $\alpha_s^2 \sim \alpha_{ew} \sim (p_t^2 - m_t^2)/m_t^2$ is only approximately satisfied since, for the invariant mass cuts adopted here, $|(p_t^2 - m_t^2)/m_t^2| \sim \delta$ can be as big as 0.5.

A set of interesting observables for the process $p\bar{p} \to J_b J_{\bar{b}} e^+ E_T + X$ are plotted in Fig. 5. Besides $M_T(t)$ and $p_T(t)$, for the s-channel-like signal we present histograms for

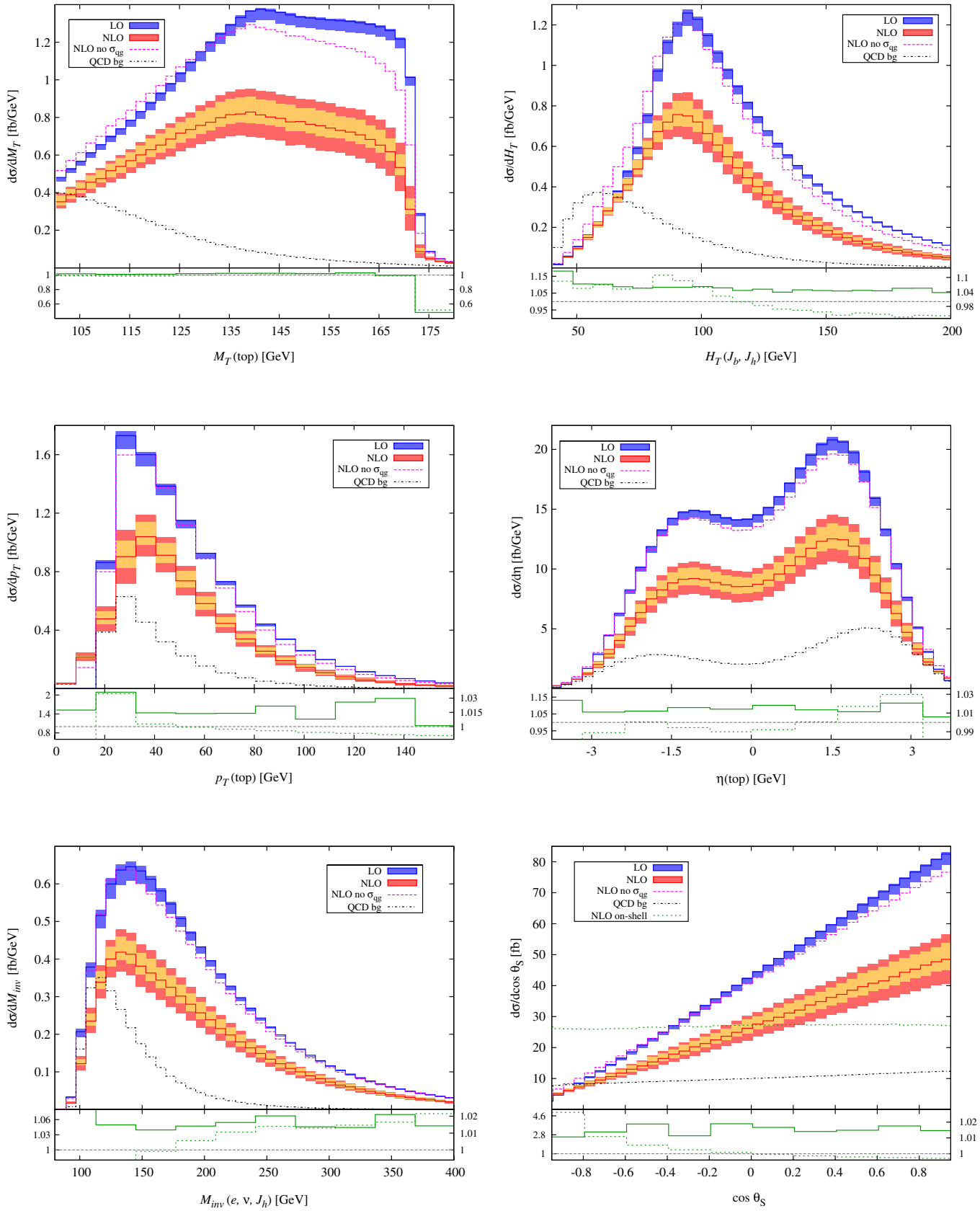

FIG. 4 (color online). Kinematical distributions for $p\bar{p} \to J_b J_l e^+ E_T + X$ at the Tevatron. Top: top quark transverse mass (left) and hadronic transverse energy (right). Center: top quark transverse momentum (left) and top quark pseudorapidity (right). Bottom: $e^+ \nu J_h$ invariant mass (left) and $\cos\theta_S$ (right). See the text for a precise definition of the observables and further explanations.

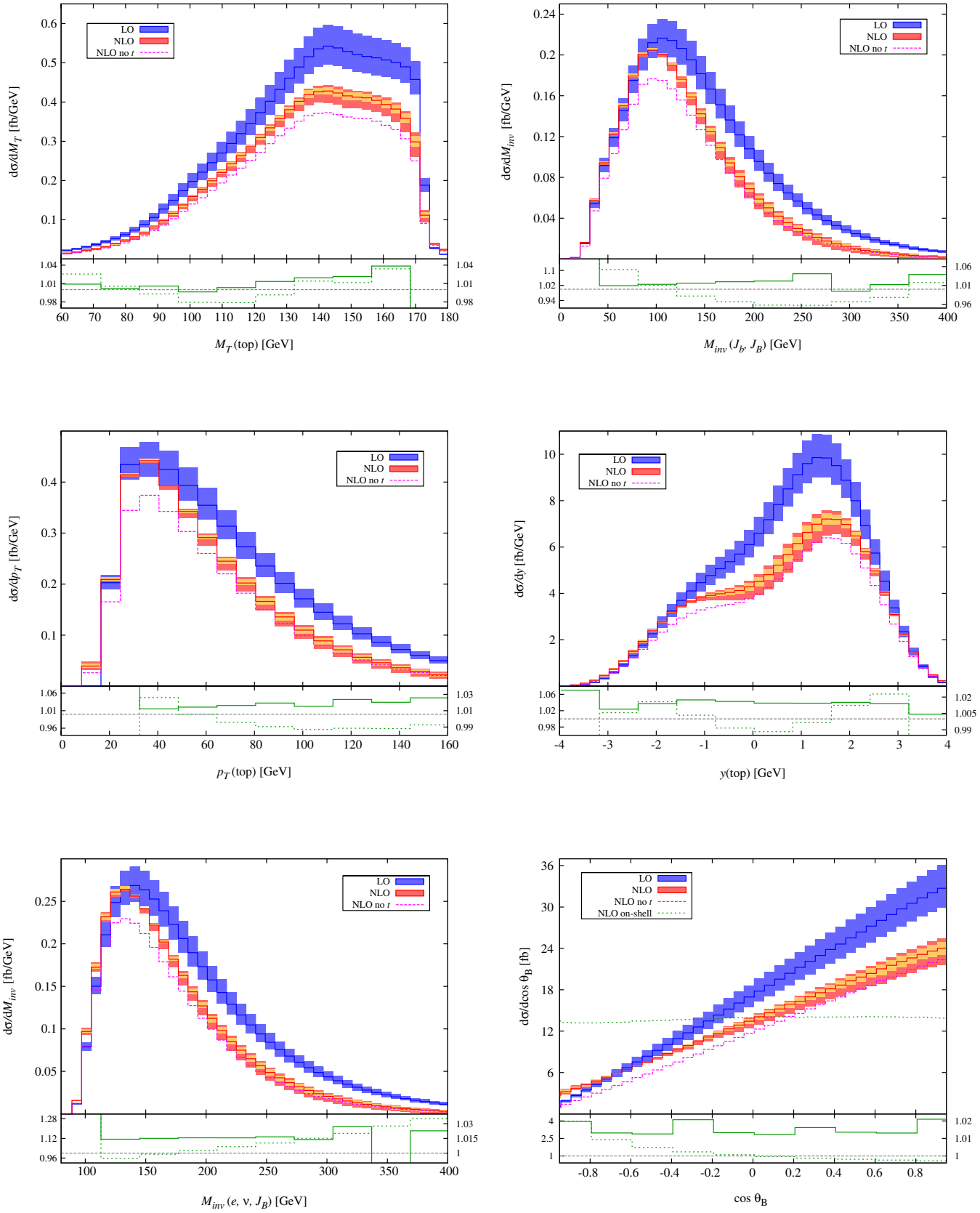

FIG. 5 (color online). Kinematical distributions for $p\bar{p} \to J_b J_{\bar{b}} e^+ E_T + X$ at the Tevatron. Top: top quark transverse mass (left) and $J_b J_{\bar{b}}$ invariant mass (right). Center: top quark transverse momentum (left) and top quark rapidity (right). Bottom: $e^+ \nu_e J_{\bar{b}}$ invariant mass (left) and $\cos\theta_B$ (right). See the text for a precise definition of the observables and further explanations.

TABLE IV. Kinematical cuts and vetoes used for LHC results.

$pp \to J_b J_l e^+ \not{E}_T + X$	$pp \to J_b J_{\bar{b}} e^+ \not{E}_T + X$
$p_T(J_b) > 20$ GeV	$p_T(J_b) > 20$ GeV
$p_T(\text{hardest } J_l) > 20$ GeV	$p_T(J_{\bar{b}}) > 30$ GeV
$p_T(\text{extra } J_{\bar{b}}) < 15$ GeV	$p_T(\text{extra } J_l) < 15$ GeV
$\not{E}_T + p_T(e) > 60$ GeV	$\not{E}_T + p_T(e) > 60$ GeV
$120 < m_{\text{inv}} < 200$ GeV	$120 < m_{\text{inv}} < 200$ GeV

TABLE V. LO and NLO cross sections for the processes (3.1) and (3.2), computed using the parameters given in Table I and imposing the kinematical cuts and vetoes given in Table IV. The errors come from scale uncertainty only. All numbers are in picobarns.

$pp \to J_b J_l e^+ \not{E}_T + X$		ET	NWA
	LO[pb]	$3.460(1)^{+0.278}_{-0.403}$	3.505(1)
	NLO[pb]	$1.609(6)^{+0.303}_{-0.240}$	1.642(1)
$pp \to J_b J_{\bar{b}} e^+ \not{E}_T + X$		ET	NWA
	LO[pb]	$0.1654(1)^{+0.0001}_{-0.0010}$	0.1677(1)
	NLO[pb]	$0.1618(4)^{+0.0021}_{-0.0005}$	0.1635(1)

$$M_{\text{inv}}(J_b, J_{\bar{b}}) \equiv \sqrt{(p(J_b) + p(J_{\bar{b}}))^2},$$
$$y(t) \equiv \frac{1}{2} \ln\left(\frac{E_t + |\vec{p}_{\parallel}(t)|}{E_t - |\vec{p}_{\parallel}(t)|}\right),$$
$$M_{\text{inv}}(e, \nu, J_{\bar{b}}) \equiv \sqrt{(p(e) + p(\nu) + p(J_{\bar{b}}))^2},$$
$$\cos\theta_B \equiv \frac{\vec{p}(e) \cdot \vec{p}(\bar{p})}{|\vec{p}(e)||\vec{p}(\bar{p})|}\bigg|_{\text{top r.f.}}, \tag{3.5}$$

where E_t denotes the energy of the reconstructed top quark and $\vec{p}(\bar{p})$ is the three-momentum of the incoming antiproton. $M_{\text{inv}}(J_b, J_{\bar{b}})$ is the invariant mass of the two b-tagged jets, $y(t)$ is the rapidity of the top quark, $M_{\text{inv}}(e, \nu, J_{\bar{b}})$ represents the misreconstructed mass of the top quark (i.e. the invariant mass obtained using the tagged bottom quark which does not come from the decay of the top quark) and $\cos\theta_B$, the angle between the final-state lepton and the antiproton beam in the top quark rest frame. As before, the solid blue and red curves represent the LO and NLO resonant result, while the three bands are obtained by scale variations, as in the case of the t-channel-like process. In this case, the dashed magenta line gives the NLO prediction without the contribution of t-channel-like diagrams, while, as before, the lower plots show the ratio of the two implementations of the NWA and the effective-theory result at NLO.

For $p\bar{p} \to J_b J_{\bar{b}} e^+ \not{E}_T + X$, the total NLO corrections are smaller than for the t-channel-like process, and about 10–20% of the LO result for most distributions in the peak region. Contrary to $p\bar{p} \to J_b J_l e^+ \not{E}_T + X$, the scale dependence of the NLO result is reduced compared to the Born prediction, though only mildly. As pointed out for the total cross section, the contribution of t-channel diagrams is quite important, even after cuts, and comparable to the effect of NLO corrections for some distributions (e.g. $M_{\text{inv}}(J_b, J_{\bar{b}})$, $p_T(t)$ and $M_{\text{inv}}(e, \nu, J_{\bar{b}})$). The nonfactorizable corrections are again generally small, and usually in the 1–3% range. Once more we point out that the two implementations of the NWA, with and without exact spin correlations, are significantly different for observables involving angles, like $\cos\theta_B$, whereas spin-correlation effects are small for most of other distributions.

B. Single-top production at the 7 TeV LHC

In this section we present results for single-top production at the LHC at a center-of-mass energy of 7 TeV. Table IV shows the kinematical cuts and vetoes applied to the two processes, $pp \to J_b J_l e^+ \not{E}_T + X$ and $pp \to J_b J_{\bar{b}} e^+ \not{E}_T + X$, in this case. The constraints are very similar to the ones used for Tevatron, except for harder cuts on the transverse missing energy and transverse lepton momentum.

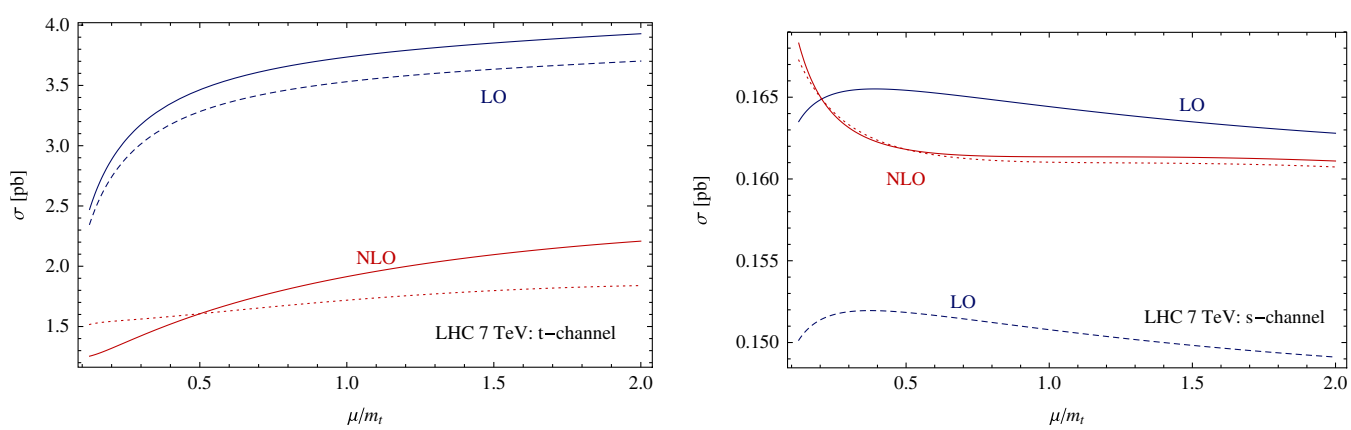

FIG. 6 (color online). Scale dependence of the total cross section for $pp \to J_b J_l e^+ \not{E}_T$ (left) and $pp \to J_b J_{\bar{b}} e^+ \not{E}_T$ (right) at the 7 TeV LHC. The plot shows the LO cross section with LO (dashed blue) and NLO (solid blue) PDFs, and the NLO cross section with simultaneous variation of factorization and renormalization scale (solid red) and for fixed factorization scale (dashed red).

Results for the total cross sections are given in Table V. The total NLO corrections amount to $\sim -53\%$ for the t-channel-like process, whereas for $pp \to J_b J_{\bar{b}} e^+ E_T + X$ they are very small ($\sim -2.5\%$). As for the Tevatron, the nonfactorizable corrections are small ($\sim 1\%$), and confirm the naïve expectation $\sim \Gamma_t/m_t$. Of the total NLO cross section for $pp \to J_b J_l e^+ E_T + X$, only 0.5% arises from s-channel diagrams. On the contrary, for $pp \to J_b J_{\bar{b}} e^+ E_T + X$, t-channel diagrams contribute about 59% of the total NLO cross section. This is a consequence of the much larger cross section of t-channel single-top production compared to s-channel production at the LHC. For the t-channel-like signal the scale dependence is only mildly reduced at NLO. Again, this can be partly explained by the additional renormalization-scale dependence introduced at this order, as is clear from the left plot in Fig. 6. For the s-channel-like signal, the scale dependence is increased at NLO. In this case, this can be explained by our default choice for the scales, $m_t/4 \leq \mu_R = \mu_F \leq m_t$, which is very close to the region where the scale dependence of the NLO cross section is the strongest and the scale dependence of the Born cross section the weakest. From the right plot in Fig. 6 it can be clearly seen that above $\mu_R = \mu_F = 0.75 m_t$ the scale dependence of the NLO result is instead very mild, and much flatter than the LO result.

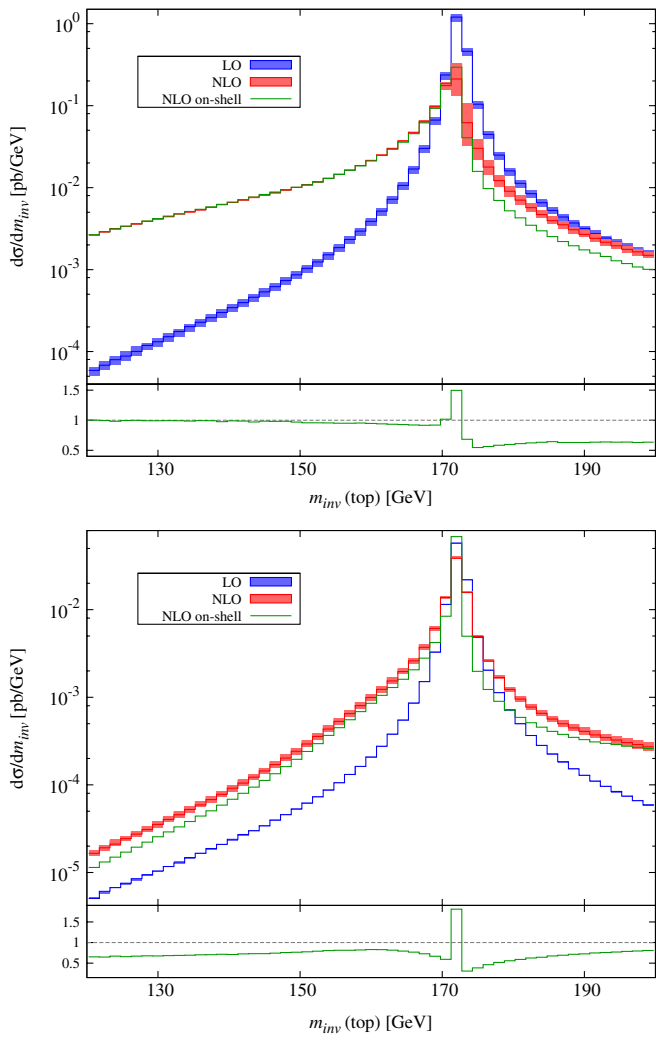

FIG. 7 (color online). Top invariant mass distributions for the process $pp \to J_b J_l e^+ E_T$ (upper plot) and $pp \to J_b J_{\bar{b}} e^+ E_T$ (lower plot) at the 7 TeV LHC. The blue band represents the LO ET result, the red band the NLO ET result, and the green curve the NLO spin-correlated NWA prediction. For the ET results the band width is obtained by varying the factorization and renormalization scales in the interval $m_t/4 \leq \mu_R = \mu_F \leq m_t$. The lower panels show the NWA result divided by the NLO ET result to illustrate the off shell effects.

Figure 7 shows plots for the top quark invariant mass distribution for the two processes. The blue band was obtained varying the scale in the LO cross section in the interval $m_t/4 \leq \mu_R = \mu_F \leq m_t$, and the red band is the analogue result for the NLO cross section. The green curve is the NLO prediction in the narrow-width approximation. As for the Tevatron, by comparing the two NLO predictions one can see that the nonfactorizable corrections are sizeable (especially for the s-channel-like process) and negative at the peak, while they turn positive above $m_{\rm inv} \sim m_t$. We again point out that the change in the sign of the nonfactorizable contributions explains the small off shell effects observed in the total cross section.

We now come to the discussion of kinematical distributions. In Fig. 8 we plot a selection of observables for the process $pp \to J_b J_l e^+ E_T + X$. The observables chosen are the same ones used for the Tevatron analysis, i.e. $M_T(t)$, $H_T(J_b, J_h)$, $p_T(t)$, $\eta(t)$, $M_{\rm inv}(e, \nu, J_h)$ and $\cos\theta_S$. As in the previous section, the blue and red solid lines are the LO and NLO effective-theory prediction for the central value of the scales, while the blue and red bands are obtained by varying the scales simultaneously in the interval $m_t/4 \leq \mu_R = \mu_F \leq m_t$. The orange band corresponds to variation of the factorization scale at fixed renormalization-scale. The dashed magenta line is the NLO result without the quark-gluon-initiated processes, and the black dot-dashed line is the contribution of tree-level QCD background diagrams. The lower plots show the ratio of the narrow-width implementation with full spin correlations (solid green line, right scale) and without (dashed green line, left scale) to the resonant result at NLO.

As for the Tevatron, the total NLO corrections are large and negative, up to $\sim$50–60% in the central bins, and they mainly arise from the gluon-initiated partonic channels. Nonfactorizable corrections are small, generally less than $\sim$5%, except close to particular kinematic thresholds. Spin-correlation effects are also small, and comparable in size to nonfactorizable corrections. An exception to this are observables depending upon angles, e.g. $\cos\theta_S$, where the difference between the two NWA implementations is very large, and where an exact treatment of spin-correlation effects is clearly necessary. Also note that at the LHC the contribution of the QCD background is smaller, compared

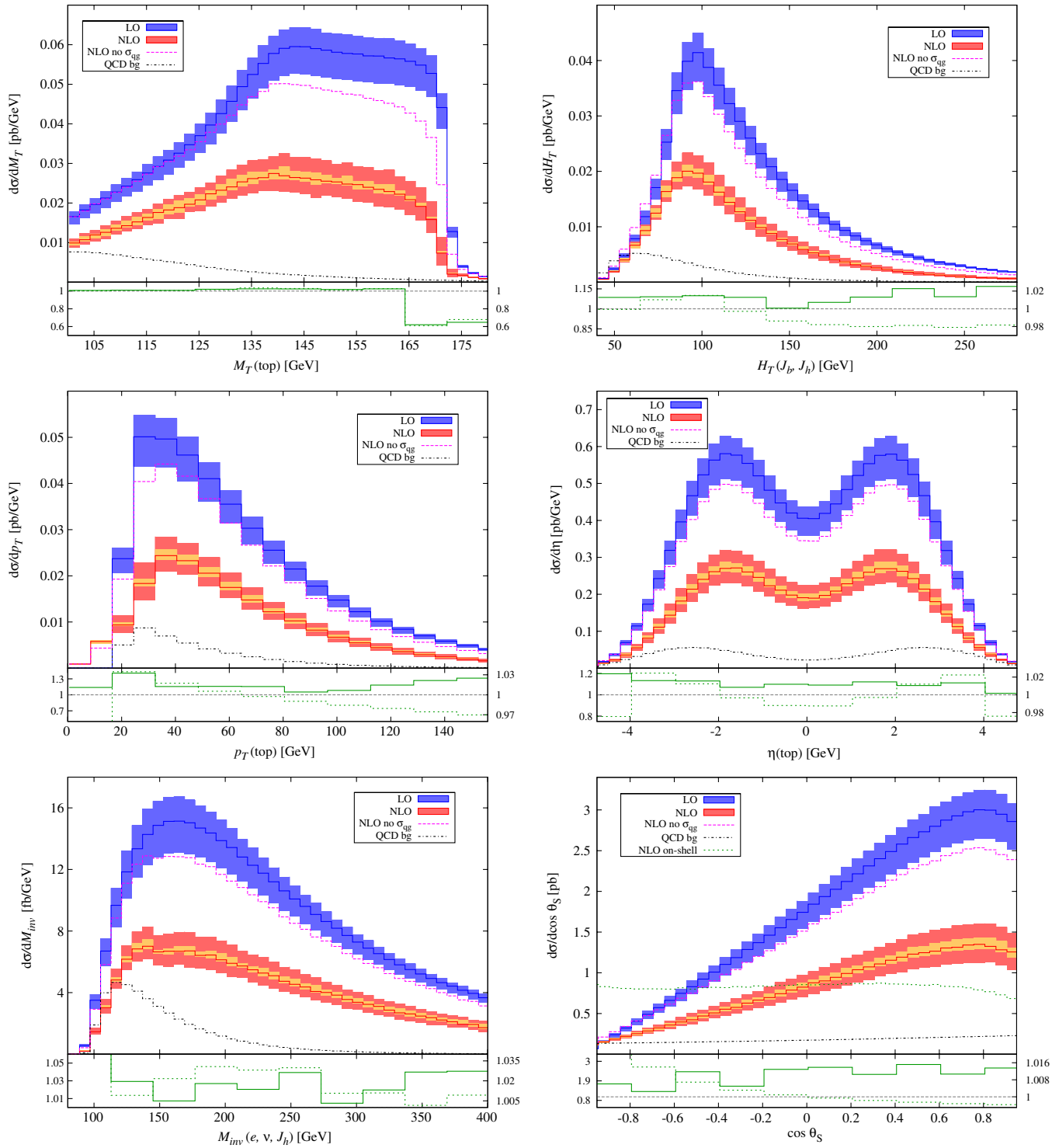

FIG. 8 (color online). Kinematical distributions for $pp \to J_b J_l e^+ E_T + X$ for the 7 TeV LHC. Top: top quark transverse mass (left) and hadronic transverse energy (right). Center: top quark transverse momentum (left) and top quark pseudorapidity (right). Bottom: $e^+ \nu J_h$ invariant mass (left) and $\cos\theta_S$ (right). See the text for a precise definition of the observables and further explanations.

to the signal, than for the Tevatron. The NLO corrections found here are generally much larger than the ones presented in Ref. [28]. Reasons for these large differences will be discussed in Sec. III D.

Kinematical distributions for $pp \to J_b J_{\bar{b}} e^+ E_T + X$ are given in Fig. 9. The observables presented are $M_T(t)$, $M_{\rm inv}(J_b, J_{\bar{b}})$, $p_T(t)$, $y(t)$, $M_{\rm inv}(e, \nu, J_{\bar{b}})$ and $\cos\theta_B$, as for the Tevatron. In this case, the dashed magenta line

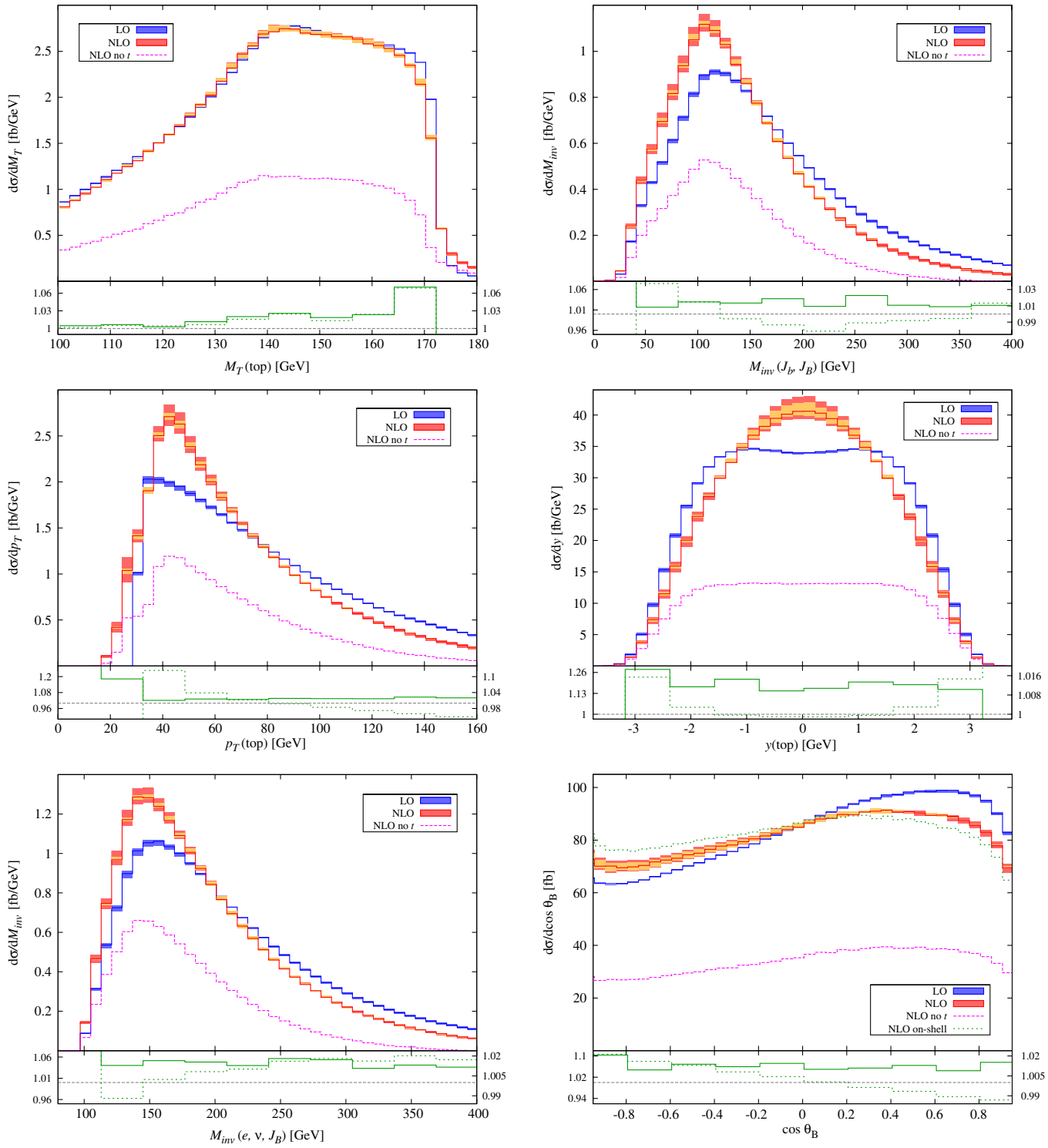

FIG. 9 (color online). Kinematical distributions for $pp \to J_b J_{\bar{b}} e^+ E_T + X$ for the 7 TeV LHC. Top: top quark transverse mass (left) and $J_b J_{\bar{b}}$ invariant mass (right). Center: top quark transverse momentum (left) and top quark rapidity (right). Bottom: $e^+ \nu_e J_{\bar{b}}$ invariant mass (left) and $\cos\theta_B$ (right). See the text for a precise definition of the observables and further explanations.

represents the NLO contribution from s-channel diagrams only. We note that the behavior of the NLO corrections for $pp \to J_b J_{\bar{b}} e^+ E_T$ at the LHC is qualitatively very different from what is observed at the Tevatron. This is a consequence of the large contributions of the t-channel diagrams. The NLO corrections arising from s-channel diagrams only are large and negative, whereas the t-channel contributions are large and positive. As a result

the total correction to the transverse mass distribution is very small. For $M_{\rm inv}(J_b, J_{\bar{b}})$, $p_T(t)$, $y(t)$ and $M_{\rm inv}(e, \nu, J_h)$ the inclusion of the t-channel contributions leads to a distortion of the shape of the distribution, with a sizeable positive total correction ($\sim 20\%$) in the peak region, and negative corrections in the tail regions. This is particularly dramatic for the rapidity distribution, where the plateaux of the LO and NLO s-channel result is completely erased by the t-channel corrections. Once more, nonfactorizable corrections are found to be small in most of the kinematical ranges considered here. The same is true for spin-correlation effects, except for the distribution for $\cos\theta_B$, as already observed for the Tevatron.

C. Effects of a nondiagonal CKM matrix

The calculations presented in this paper so far have assumed that the CKM matrix is diagonal. However, if we consider processes proportional to the off diagonal elements of the matrix we can observe some interesting results. In particular, the shape of the top quark rapidity distribution is highly dependent on the flavor of the initial-state partons. This effect has been discussed, at tree-level, in Ref. [38].

The results shown in Fig. 10, for t-channel production at the LHC, show good agreement to those found in Ref. [38] at leading-order. The events in which the initial-state parton is a bottom quark are more central than those in which the initial-state parton is a down quark. The size of the next-to-leading-order effects means their impact on the overall shape of the distributions is negligible. The tree-level differences still dominate. However, it is worth noting that for the contributions proportional to $|V_{td}|^2$, the inclusion of next-to-leading-order effects seems to broaden the distribution, further accentuating the differences in event centrality between bottom quark and down quark initiated events.

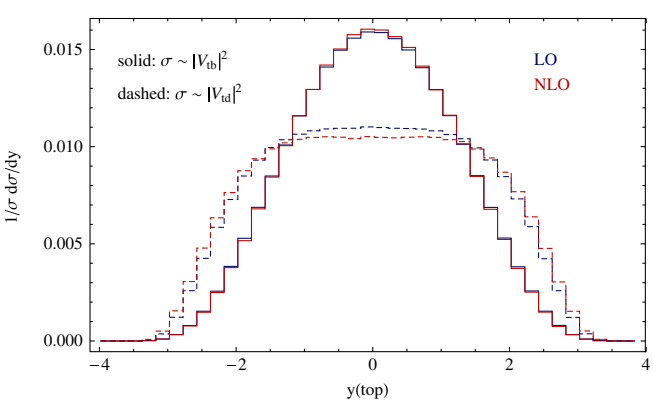

FIG. 10 (color online). Normalized top quark rapidity distributions for t-channel production at the LHC. Leading-order results are shown in blue and next-to-leading-order results in red. Solid and dashed lines represent contributions proportional to $|V_{tb}|^2$ and $|V_{td}|^2$, respectively.

The main focus of this paper is the NLO corrections to single-top production processes, and we have seen that their impact on the shapes of these distributions is negligible in comparison to the large differences observed at leading-order; further discussion of the effects of a non-diagonal CKM matrix will not be made in this paper.

D. Comparison to earlier results

As mentioned in Sec. III B, the size of the NLO corrections presented here are, in general, much larger than those presented in, for example, Ref. [28]. This is a consequence of the different kinematical cuts chosen and, in particular, of the strong veto imposed on extra b-tagged jets. As a validity check, we performed our calculations again for t-channel production at the LHC, this time using a different set of kinematical cuts and no veto on extra b-tagged jets. Also, in this section we have evaluated the LO results using LO parton distributions. A list of the cuts used is given in Table VI.

Our results, calculated with these less stringent cuts, are shown in Fig. 11. Although a different set of kinematical cuts were used, it is clear to see by comparison to the results shown in Fig. 8, that removing the veto on the extra b-tagged jets leads to a large reduction in the size of the NLO contributions. The size of these corrections are also in much better agreement with those found in Ref. [28].

The major factor contributing to the strong correlation between the veto on extra b-tagged jets and the size of the NLO corrections are the diagrams with initial-state q and g partons which result in a final state containing both a b and a $\bar{b}$ quark. When using our original cuts and vetoes (diagrams in Fig. 8) the NLO contribution to the total cross section due to these diagrams amounted to a negative correction of $\sim$40% of the leading order value. This can clearly be seen in the diagrams by comparing the full NLO result (red lines) to the NLO result with the qg contribution removed (dashed magenta lines). When we move to our less stringent cuts, however, the NLO contribution to the total cross section due to the qg diagrams is reduced to a negative correction of $\sim$10% of the leading-order value. These diagrams still have a large impact on the size of the NLO corrections but their importance is substantially reduced in comparison to the case where we employed a strong veto.

TABLE VI. Kinematical cuts used for comparison to earlier results.

$p\bar{p} \to J_b J_l e^+ E_T + X$	
$p_T(J_b) > 20$ GeV	$E_T > 20$ GeV
$p_T(\text{hardest } J_l) > 20$ GeV	$\eta(J_b) < 2.5$
$p_T(e) > 20$ GeV	$\eta(\text{hardest } J_l) < 2.0$
$120 < m_{\rm inv} < 200$ GeV	$\eta(e) < 2.5$

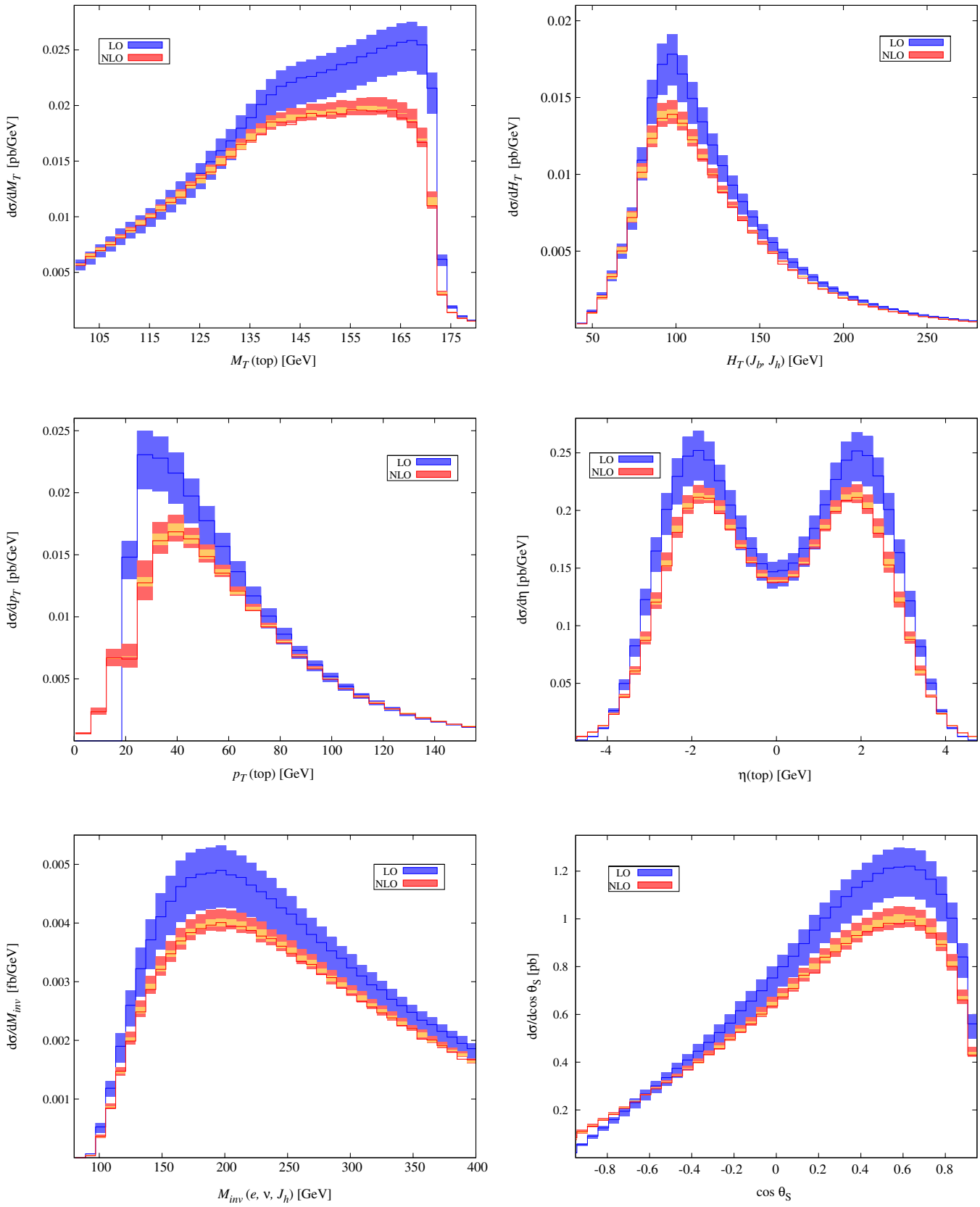

FIG. 11 (color online). Kinematical distributions for $pp \to J_b J_l e^+ E_T + X$ for the 7 TeV LHC with the cuts shown in Table VI applied. Top: top quark transverse mass (left) and hadronic transverse energy (right). Center: top quark transverse momentum (left) and top quark pseudorapidity (right). Bottom: $e^+ \nu J_h$ invariant mass (left) and $\cos\theta_S$ (right). See the text for a precise definition of the observables and further explanations.

IV. CONCLUSION

We have applied a general method to include nonfactorizable corrections for processes at hadron colliders to single-top production in the t- and s-channels. Within this effective-theory inspired method, nonfactorizable corrections are nothing but corrections due to soft modes. The corrections to the production and decay parts of the process are reproduced by hard effects. This method allows us to include off shell effects with a minimal amount of computation. Of course, spin-correlation effects are also fully included.

As is well known, spin-correlation effects can be very large for particular kinematic distributions. On the other hand, off shell effects are generally found to be small. For the total cross section and most distributions they amount to a correction of the order of 1–3%. However, they can be substantially larger for observables that are not inclusive enough in the invariant mass of the decay products of the top quark. Apart from the invariant mass distribution itself, this is manifested at kinematic edges of certain distributions.

Thus, even though off shell effects are small, they can have an impact on precise measurements of the top quark mass. Furthermore, we stress that we have evaluated the soft (nonfactorizable) corrections with the same large scale, $\mu_h \sim m_t$, as the hard corrections. Naively, changing the scale of the soft corrections from μ_h to $\mu_s \sim \Gamma_t$ would lead to a substantial increase in their importance. However, a more careful study is required for a consistent resummation of $\log \mu_s/\mu_h$. We are confident that these, and related questions, are best addressed within an effective-theory framework.

ACKNOWLEDGMENTS

This work has been supported in part by the European Commission through the Initial Training Network PITN-GA-2010-264564 (LHCPhenoNet). P. F. acknowledges support by the ''Stichting voor Fundamenteel Onderzoek der Materie (FOM)''. F. G. was supported, in part, by the EU Contract No. MRTN-CT-2006-035482, FLAVIAnet and by the grant Borse di ricerca in collaborazione internazionale by Regione Puglia, Italy. P. M. is supported by an STFC studentship. P. F. and F. G. thank the IPPP, Durham for their kind hospitality during part of this work.

[1] T. Aaltonen *et al.* (The CDF collaboration), Phys. Rev. Lett. **103**, 092002 (2009).
[2] V. M. Abazov *et al.* (D0 Collaboration), Phys. Rev. Lett. **103**, 092001 (2009).
[3] J. Alwall *et al.*, Eur. Phys. J. C **49**, 791 (2007).
[4] G. Mahlon and S. J. Parke, Phys. Lett. B **476**, 323 (2000).
[5] P. Motylinski, Phys. Rev. D **80**, 074015 (2009).
[6] T. M. P. Tait and C.-P. Yuan, Phys. Rev. D **63**, 014018 (2000).
[7] Q.-H. Cao, J. Wudka, and C.-P. Yuan, Phys. Lett. B **658**, 50 (2007).
[8] M. Dittmar and H. K. Dreiner, Phys. Rev. D **55**, 167 (1997).
[9] W. Bernreuther, J. Phys. G **35**, 083001 (2008).
[10] G. Bordes and B. van Eijk, Nucl. Phys. **B435**, 23 (1995).
[11] T. Stelzer, Z. Sullivan, and S. Willenbrock, Phys. Rev. D **56**, 5919 (1997).
[12] M. C. Smith and S. Willenbrock, Phys. Rev. D **54**, 6696 (1996).
[13] W. T. Giele, S. Keller, and E. Laenen, Phys. Lett. B **372**, 141 (1996).
[14] S. Zhu, Phys. Lett. B **524**, 283 (2002); **537**, 351(E) (2002).
[15] B. W. Harris, E. Laenen, L. Phaf, Z. Sullivan, and S. Weinzierl, Phys. Rev. D **66**, 054024 (2002).
[16] Z. Sullivan, Phys. Rev. D **70**, 114012 (2004).
[17] M. Beccaria *et al.*, Phys. Rev. D **77**, 113018 (2008).
[18] G. Macorini, S. Moretti, and L. Panizzi, Phys. Rev. D **82**, 054016 (2010).
[19] N. Kidonakis, Phys. Rev. D **75**, 071501 (2007).
[20] N. Kidonakis, Phys. Rev. D **81**, 054028 (2010).
[21] H. X. Zhu, C. S. Li, J. Wang, and J. J. Zhang, J. High Energy Phys. 02 (2011) 099.
[22] J. Wang, C. S. Li, H. X. Zhu, and J. J. Zhang, arXiv:1010.4509.
[23] J. M. Campbell, R. K. Ellis, and F. Tramontano, Phys. Rev. D **70**, 094012 (2004).
[24] Q. H. Cao and C. P. Yuan, Phys. Rev. D **71**, 054022 (2005).
[25] Q. H. Cao, R. Schwienhorst, J. A. Benitez, R. Brock, and C. P. Yuan, Phys. Rev. D **72**, 094027 (2005).
[26] J. M. Campbell and F. Tramontano, Nucl. Phys. **B726**, 109 (2005.
[27] S. Heim, Q. H. Cao, R. Schwienhorst, and C. P. Yuan, Phys. Rev. D **81**, 034005 (2010).
[28] R. Schwienhorst, C. P. Yuan, C. Mueller, and Q. H. Cao, Phys. Rev. D **83**, 034019 (2011).
[29] P. Falgari, P. Mellor, and A. Signer, Phys. Rev. D **82**, 054028 (2010).
[30] R. Pittau, Phys. Lett. B **386**, 397 (1996).
[31] W. Beenakker, A. P. Chapovsky, and F. A. Berends, Nucl. Phys. **B508**, 17 (1997).
[32] A. Denner, S. Dittmaier, and M. Roth, Nucl. Phys. **B519**, 39 (1998).
[33] N. Kauer and D. Zeppenfeld, Phys. Rev. D **65**, 014021 (2001).
[34] V. S. Fadin, V. A. Khoze, and A. D. Martin, Phys. Rev. D **49**, 2247 (1994).
[35] K. Melnikov and O. I. Yakovlev, Phys. Lett. B **324**, 217 (1994).

[36] J. M. Campbell, R. Frederix, F. Maltoni, and F. Tramontano, Phys. Rev. Lett. **102**, 182003 (2009).
[37] J. M. Campbell, R. Frederix, F. Maltoni, and F. Tramontano, J. High Energy Phys. 10 (2009) 042.
[38] J. A. Aguilar-Saavedra and A. Onofre, arXiv:1002.4718.
[39] S. Frixione, E. Laenen, P. Motylinski, and B. R. Webber, J. High Energy Phys. 03 (2006) 092.
[40] S. Frixione, E. Laenen, P. Motylinski, B. R. Webber, and C. D. White, J. High Energy Phys. 07 (2008) 029.
[41] S. Alioli, P. Nason, C. Oleari, and E. Re, J. High Energy Phys. 09 (2009) 111; 02 (2010) 011.
[42] E. Re, Eur. Phys. J. C **71**, 1547 (2011).
[43] M. Beneke, A. P. Chapovsky, A. Signer, and G. Zanderighi, Nucl. Phys. **B686**, 205 (2004).
[44] R. G. Stuart, Phys. Lett. B **262**, 113 (1991).
[45] A. Aeppli, G. J. van Oldenborgh, and D. Wyler, Nucl. Phys. **B428**, 126 (1994).
[46] A. Denner, S. Dittmaier, M. Roth, and L. H. Wieders, Nucl. Phys. **B724**, 247 (2005).
[47] M. Beneke and V. A. Smirnov, Nucl. Phys. **B522**, 321 (1998).
[48] V. A. Smirnov, Springer Tracts Mod. Phys. **177**, 1 (2002).
[49] A. P. Chapovsky, V. A. Khoze, A. Signer, and W. J. Stirling, Nucl. Phys. **B621**, 257 (2002).
[50] M. Beneke, P. Falgari, C. Schwinn, A. Signer, and G. Zanderighi, Nucl. Phys. **B792**, 89 (2008).
[51] S. Actis, M. Beneke, P. Falgari, and C. Schwinn, Nucl. Phys. **B807**, 1 (2009).
[52] S. Catani and M. H. Seymour, Nucl. Phys. **B485**, 291 (1997); **B510**, 503(E) (1998).
[53] S. Frixione, Z. Kunszt, and A. Signer, Nucl. Phys. **B467**, 399 (1996).
[54] A. D. Martin, W. J. Stirling, R. S. Thorne, and G. Watt, Eur. Phys. J. C **63**, 189 (2009).